

Article

Atomic Structure of Mn-Doped CoFe_2O_4 Nanoparticles for Metal–Air Battery Applications

Katariina Pussi ^{1,2,*}, Keying Ding ³, Bernardo Barbiellini ^{1,4}, Koji Ohara ^{5,6}, Hiroki Yamada ⁵,
Chuka Onuh ³, James McBride ⁷, Arun Bansil ⁴, Ray K. Chiang ⁸ and Saeed Kamali ^{9,10,*}

¹ Physics Department, School of Engineering Science, LUT University, 53851 Lappeenranta, Finland

² Production Systems, Natural Resources Institute Finland (Luke), 00790 Helsinki, Finland

³ Department of Chemistry, Middle Tennessee State University, Murfreesboro, TN 37132, USA

⁴ Physics Department, Northeastern University, Boston, MA 02115, USA

⁵ Diffraction and Scattering Division, Center for Synchrotron Radiation Research, Japan Synchrotron Radiation Research Institute (JASRI, SPring-8), 1-1-1 Kouto, Sayo-cho, Hyogo, Sayo-gun 679-5198, Japan

⁶ Faculty of Materials for Energy, Shimane University, 1060, Nishi-Kawatsu-Cho, Matsue 690-8504, Japan

⁷ Chemistry Department, Vanderbilt University, Nashville, TN 37235, USA

⁸ Nanomaterials Laboratory, Far East University, Hsing-Shih, Tainan 74448, Taiwan

⁹ Department of Mechanical, Aerospace and Biomedical Engineering, University of Tennessee Space Institute, Tullahoma, TN 37388, USA

¹⁰ Department of Physics and Astronomy, Middle Tennessee State University, Murfreesboro, TN 37132, USA

* Correspondence: katariina.pussi@lut.fi (K.P.); skamalim@utk.edu (S.K.)

Abstract: We discuss the atomic structure of cobalt ferrite nanoparticles doped with Mn via an analysis based on combining atomic pair distribution functions with high energy X-ray diffraction and high-resolution transmission electron microscopy measurements. Cobalt ferrite nanoparticles are promising materials for metal–air battery applications. Cobalt ferrites, however, generally show poor electronic conductivity at ambient temperatures, which limits their bifunctional catalytic performance in oxygen electrocatalysis. Our study reveals how the introduction of Mn ions promotes the conductivity of the cobalt ferrite electrode.

Keywords: cobalt ferrite nanoparticles; metal–air battery; oxygen reduction reaction (ORR); oxygen evolution reaction (OER); spinel oxide; Mn doping; high energy X-ray diffraction (HE-XRD); electrodes; pair distribution function (PDF) analysis



Citation: Pussi, K.; Ding, K.; Barbiellini, B.; Ohara, K.; Yamada, H.; Onuh, C.; McBride, J.R.; Bansil, A.; Chiang, R.K.; Kamali, S. Atomic Structure of Mn-Doped CoFe_2O_4 Nanoparticles for Metal–Air Battery Applications. *Condens. Matter* **2022**, *8*, 49. <https://doi.org/10.3390/condmat8020049>

Academic Editors: Alan R. Bishop and Antonio Bianconi

Received: 17 March 2023

Revised: 2 May 2023

Accepted: 17 May 2023

Published: 24 May 2023



Copyright: © 2022 by the authors. Licensee MDPI, Basel, Switzerland. This article is an open access article distributed under the terms and conditions of the Creative Commons Attribution (CC BY) license (<https://creativecommons.org/licenses/by/4.0/>).

1. Introduction

Oxygen reduction (ORR) and oxygen evolution (OER) reactions are the key anchors underlying the electrocatalysis processes in energy systems such as metal–air batteries and fuel cells [1,2]. ORR and OER are sluggish electrochemical reactions that require a large quantity of precious metals as catalysts for enhancing activity and durability. Achieving reversibility in the OER/ORR couple remains one of the critical materials science challenges for improved device performance. For example, Pt alloys are an effective catalyst for the ORR but not for the OER due to the formation of a Pt oxide surface film at high potential, which degrades activity. Similarly, IrO_2 is the most active catalyst for the OER due to its favorable electrical and ionic conductivities, but it is not good for the ORR. These materials problems, along with the cost and scarcity of precious metals, have hampered the development of reversible electrochemical devices. The need for a single high-performance nonprecious metal catalyst (NPMC), which is active for both ORR and OER (i.e., a bifunctional catalyst), to replace the precious metal catalysts in wide current use is thus clear.

FeN_xC active sites appear to be among the most promising NPMCs [3,4]. These catalysts can be viewed as biomimetic analogs of the heme moiety. Note that the carbon scaffolding supporting the active sites here lacks ORR activity, but the addition of N

atoms generates some ORR activity, and further addition of Fe atoms significantly boosts it. Although N-doped carbon-based NPMCs have shown remarkable ORR activity, their activity and durability for the OER remain insufficient. In fact, compared to the ORR, the OER is more challenging due to the extremely oxidative conditions at high potentials, where most of the currently studied carbon-based catalysts degrade due to rapid oxidation of carbon. Given the intrinsic stability of metal-based transition metal oxides, such as cobalt ferrite (CoFe_2O_4), ORR and OER oxide catalysts could replace the carbon-based catalysts for reversible electrochemical technologies [1,2]. Cobalt ferrite is known to adopt the inverse spinel structure, where half of Fe^{3+} ions are located at the tetrahedral sites (A-sites), while the octahedral sites (B-sites) host the remaining Fe^{3+} and Co^{2+} ions [5], some deviations from this ideal structure notwithstanding [6].

The key materials challenge that needs to be addressed in this connection is that most oxide materials show poor electronic conductivity at ambient temperatures, which limits their bifunctional catalytic performance in oxygen electrocatalysis. In particular, CoFe_2O_4 is a ferrimagnetic insulator [6,7]. An approach toward solving this problem is to modify the oxide matrix with Mn dopants. Here we focus on the structural aspects of these nanoparticles in order to identify their structural features that could promote their ORR/OER activity. In this way, one can engineer Mn doping [5] along the lines of conventional doping in semiconductor technology to achieve electronic control of redox chemistry of cobalt ferrite for bifunctional catalysis. We specifically investigate a series of monodispersed Co–Mn ferrite samples with composition $\text{Co}_{1-x}\text{Mn}_x\text{Fe}_2\text{O}_4$, where $x = 0.00, 0.25, 0.50, 0.75, \text{ and } 1.00$.

2. Synthesis, Characterizations, and HE-XRD Experiments

Iron (III) oxide monohydrate ($\alpha\text{-Fe}_2\text{O}_3 \cdot \text{H}_2\text{O}$, 99.9%), cobalt (II, III) oxide (Co_3O_4 , 99.5%), and manganese (II) oxide (MnO , 99%) were purchased from Strem Chemical. Oleic acid (technical grade, 90%) and benzyl ether (98%) were purchased from Sigma Aldrich. All chemicals were used without further purification. Synthesis of mixed-metal oleate complexes ($\text{Co}_{1-x}\text{Mn}_x\text{Fe}_2\text{-oleate}$, $x = 0.00, 0.25, 0.50, 0.75, \text{ and } 1.00$) proceeded as follows. In a typical reaction, a 100 mL three-necked round bottom flask was loaded with $\alpha\text{-Fe}_2\text{O}_3 \cdot \text{H}_2\text{O}$ (12 mmol, 2.13 g), Co_3O_4 (2 mmol, 482 mg), MnO (6 mmol, 426 mg), and oleic acid (48 mL). A water-cooled condenser was attached on top of the flask. The flask was heated to 295 °C at a rate of 15 °C/min under a continuous flow of N_2 . During the reaction process, the reactants bubbled vigorously, and the color of the reaction mixture gradually changed to brown. After 4 h, the resulting brown grease-like product was allowed to cool to room temperature and was then diluted with a mixture of hexane and acetone (1:20) and centrifuged at a speed of 5000–10,000 rpm. The precipitate was washed with acetone and dried at a temperature of 60 °C for 24 h. The Co–Mn ferrite nanoparticles (NPs) ($\text{Co}_{1-x}\text{Mn}_x\text{Fe}_2\text{O}_4$, $x = 0.00, 0.25, 0.50, 0.75, \text{ and } 1.00$) were synthesized as follows. In a typical reaction for making $\text{Co}_{0.5}\text{Mn}_{0.5}\text{Fe}_2\text{O}_4$, a mixture of $\text{Co}_{0.5}\text{Mn}_{0.5}\text{Fe}_2\text{-oleate}$ complex (1.81 g), oleic acid (4.52 g), and benzyl ether (36 mL) was loaded into a 100 mL three-necked round-bottom flask. The reaction mixture was stirred very slowly to dissolve all materials at 60 °C and was then heated to 298 °C at a rate of 15 °C/min under a continuous flow of N_2 and maintained at this temperature for 2 h. The color of the reactants changed from brown to black, indicating the decomposition of the metal complex to NPs. The resulting product was diluted with a mixture of hexane and acetone (1:20) and centrifuged at a speed of 5000 rpm. Finally, the precipitate was washed twice by hexane/acetone (1:5) to produce a dark red powder, which was dried at room temperature for further characterizations.

HE-XRD measurements were performed with a photon wavelength of 0.21 Å in the transmission mode at beamline BL04B2 of the Japanese synchrotron facility SPring-8. An ionization chamber was used for monitoring the intensity of the incident X-rays, while four CdTe and three Ge detectors were used for monitoring the intensity of the scattered X-rays. A two-axis diffractometer installed at BL04B2 was used to cover the low Q (small angle) region ($\approx 0.1 \text{ \AA}^{-1}$). The setup for HE-XRD at this beamline is described in more

detail elsewhere [8,9]. To achieve a high real-space resolution, the data over the full 2θ range of the structure factor (up to 25.6 \AA^{-1}) was used in the analysis of the structure. High-Resolution Transmission Electron Microscopy (HR-TEM) and STEM-EDXS were performed on a Tecnai Osiris TEM/STEM with an operating voltage of 200 kV. Drift-corrected STEM-EDS maps were acquired using Bruker Esprit software version 1.9 utilizing a probe current on the order of 1 nA. The samples for HR-TEM were prepared by suspending the particles in isopropanol and drop-casting them on to carbon-coated copper grid. An FEI XL30-SFEG scanning electron microscopy device operating at 5 kV was used for the EDXS measurements. Figure 1 gives the HR-TEM images for all investigated samples. All samples except CoFe_2O_4 look spherical and have similar sizes. CoFe_2O_4 NPs have a larger size and cubic shape.

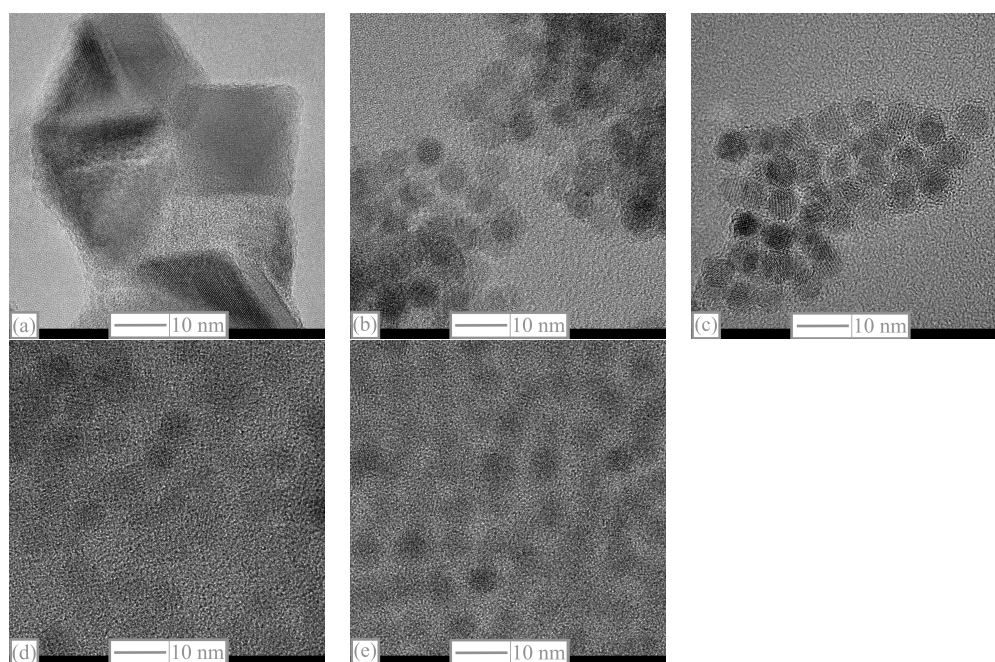


Figure 1. HR-TEM images for all investigated samples: (a) CoFe_2O_4 , (b) $\text{Co}_{0.75}\text{Mn}_{0.25}\text{Fe}_2\text{O}_4$, (c) $\text{Co}_{0.50}\text{Mn}_{0.50}\text{Fe}_2\text{O}_4$, (d) $\text{Co}_{0.25}\text{Mn}_{0.75}\text{Fe}_2\text{O}_4$, (e) MnFe_2O_4 .

The sizes and distributions of all NPs, measured using FIJI software [10], are summarized in Table 1.

Table 1. Sizes and distributions of all nanoparticles as indicated.

NPs	CoFe_2O_4	$\text{Co}_{0.75}\text{Mn}_{0.25}\text{Fe}_2\text{O}_4$	$\text{Co}_{0.50}\text{Mn}_{0.50}\text{Fe}_2\text{O}_4$	$\text{Co}_{0.25}\text{Mn}_{0.75}\text{Fe}_2\text{O}_4$	MnFe_2O_4
Size (nm)	32 ± 7	5.0 ± 0.7	5.1 ± 0.6	6.4 ± 1.0	6.0 ± 0.9

Elemental analysis results (not shown) indicate that the composition of the metal ions in our ferrite nanocrystallites agrees with that of the original precursors. Thermogravimetric analysis shows that the cobalt-rich nanocrystalline ferrites have higher thermal stability, which results in the formation of a larger particle size.

We apply the HE-XRD measurements combined with the atomic pair distribution function (PDF) technique [11] to unravel the atomic structure of the $\text{Co}_{1-x}\text{Mn}_x\text{Fe}_2\text{O}_4$ nanoparticles. We use our experimental HE-XRD data to obtain PDFs. The first step is to get the total structure factor, also called the Faber–Ziman total structure factor [12], $S(Q)$, which is a function of the absolute wave number Q ($Q = |Q| = (4\pi/\lambda)\sin\theta$), where λ is

the wavelength of the incident X-rays and θ is the scattering angle. $S(Q)$ is related to the coherent part ($I^{coh}(Q)$) of the diffraction data [13] as follows:

$$S(Q) = 1 + \frac{I^{coh}(Q) - \sum C_i |f_i(Q)|^2}{|\sum C_i f_i(Q)|^2}, \quad (1)$$

where $f_i(Q)$ is the atomic scattering factor and C_i is the concentration of the atomic species of type i . The reduced PDF, denoted $G(r)$, is given by the Fourier transform of $Q[S(Q) - 1]$:

$$G(r) = \frac{2}{\pi} \int_{Q_{min}}^{Q_{max}} Q[S(Q) - 1] \sin(Qr) dQ, \quad (2)$$

where $G(r)$ is defined by the formula

$$G(r) = 4\pi r[(\rho(r) - \rho_0)]. \quad (3)$$

Here, ρ_0 is the atomic number density of the material, and $\rho(r) = \rho_0 g(r)$ is the atomic pair density proportional to the PDF, denoted $g(r)$. The peaks of $G(r)$ and $g(r)$ are associated with atomic distances. Note that in order to improve the spatial resolution of $G(r)$, $S(Q)$ must be measured with a higher Q cut-off, Q_{max} , which becomes possible due to the higher photon energies available in the HE-XRD technique. The PDF approach has been shown to be an effective method for determining the structures of non-crystalline and disordered materials as well as nanoparticles [13–34].

Figure 2 shows our experimental data for $G(r)$, which is seen to be in good agreement with the corresponding results of Tiano et al. [35]. This consistency demonstrates the reproducibility of the HE-XRD experiment. Interestingly, the numerical values of $G(R)$ expressed in \AA^{-2} units are also comparable with the findings of Michel et al. [36] for the ferrihydrite.

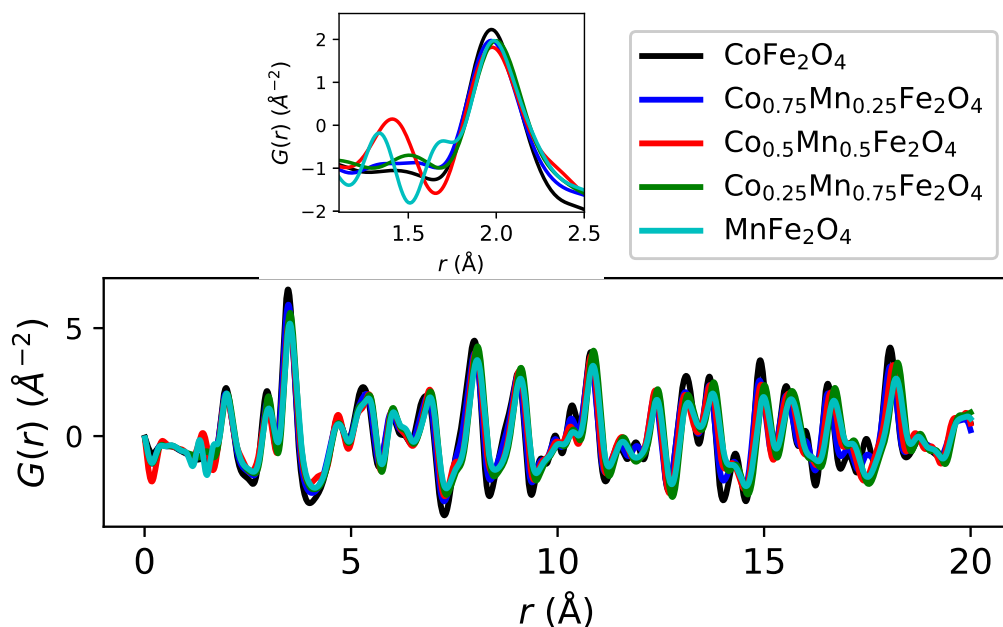


Figure 2. Experimental $G(r)$ data for all investigated samples. The top panel highlights the short-distance region.

3. Reverse Monte Carlo Analysis and Results

Constructing a starting model for refinement in an amorphous material is not a simple task because of the large number of atoms needed to resolve structural details. The Reverse Monte Carlo (RMC) method [37] finds the atomic structure directly from experimental data. RMC differs from other techniques since it is driven by the experimental data rather than

the parameters obtained, for example, through molecular dynamics simulations. For this reason, further constraints are often added to the RMC-based modeling. These constraints include closest distance windows, coordination numbers, bond angles, and model-specific polyhedral constraints. Throughout an RMC simulation, positions of atoms fluctuate similar to thermal motions [37].

The RMC method can provide snapshot views of about 10^4 atoms, which is much larger than the number of atoms conventionally used in first-principles simulations [38,39], although efficient exploitation of high-performance computing resources is continuing to extend the reach of these precise computational methods to increasingly larger molecular and condensed matter systems [40]. If the RMC fit is consistent with all the data available, then the resulting configuration will accurately capture the structural characteristics of the sample being studied. Along these lines, Pussi et al. [39] have shown how the atomic structure of the FeCrMoCBY metallic glass can be resolved by combining density functional theory (DFT) calculations with a PDF analysis.

The present experimental PDF data for Mn-doped cobalt ferrite was analyzed using the RMCProfile software [41] to model the experimental $G(r)$ profiles. The structure is modelled by a cubic cluster containing 448 atoms without periodic boundary conditions. Tiano and collaborators [35] have fitted PDFs of ferrite nanoparticles as bulk PDFs attenuated by an envelope function that reflects the size of the nanoparticles. Their results clearly demonstrate that the salient PDF features in ferrite nanoparticles are bulk-like in nature.

The optimization process was started by using the pristine CoFe_2O_4 structure. The cut-off lengths for the starting compound, CoFe_2O_4 , were 1.2, 1.70, 1.70, 2.60, 2.60, and 2.60 Å for the O–O, O–Fe, O–Co, Fe–Fe, Fe–Co, and Co–Co atomic pairs, respectively. During the optimization, atoms were allowed to move and swap within the computational cube. The PDF and partial PDF fits are shown in Figures 3 and 4, respectively, while Figure 5 illustrates the optimized atomic structures. The partial PDFs shown in Figure 4 reveal that the Co-rich and Mn-rich samples exhibit different behavior with respect to the occupation of the Co and Mn atoms in the tetrahedral and octahedral sites of the spinel lattice.

After the Monte Carlo optimization, our RMCProfile simulations yielded the following coordination for the Mn atoms: for 25% Mn doping (76 Mn–O bonds and 32 Fe–Mn bonds), the average coordination was 6.75; for 50% Mn (142 Mn–O bonds and 36 Mn–Fe bonds), the average coordination was 5.5; for 75% Mn (192 Mn–O bonds and 0 Mn–Fe bonds), the coordination was 4. Mn coordination is thus seen to decrease with increasing Mn concentration. This trend is consistent with the observations of Sanna et al. [42] and DFT simulations [5], which indicate that Mn ions prefer to substitute Co ions at the octahedral sites for $x < 0.25$, while at higher Mn concentrations, the Mn ions prefer tetrahedral sites with coordination of 4.

As we already pointed out, the key problem is the poor electronic conductivity of cobalt ferrite electrodes [1,2], which limits their electrocatalytic performance. The DFT calculations [5] show that the introduction of Mn ions can improve the conductivity of cobalt ferrite. The density of states (DOS) for Mn doping of $x = 0.5$ and $x = 1$ produces semiconductors with band gaps of 0.16 eV and 0.18 eV, respectively, which are smaller than the band gap of 2.31 eV [7] for the pristine material (CoFe_2O_4). $x = 0.75$ yields a half-metal. The total magnetic moment is found to increase with increasing x [5].

A closer look to the inset of Figure 2 reveals peaks in the experimental $G(R)$ near 1.20 Å, which is the bond length of the O_2 diatomic molecule that can bind at the surface of cobalt ferrite nanoparticles. DFT calculations [43] show that an oxygen diatomic molecule interacts with the (001) surface of cobalt ferrite on top of an exposed octahedrally coordinated metal ion. Since our model cluster does not include the oxygen diatomic molecule, this surface effect must be added as has been done previously in gold nanoparticles [44].

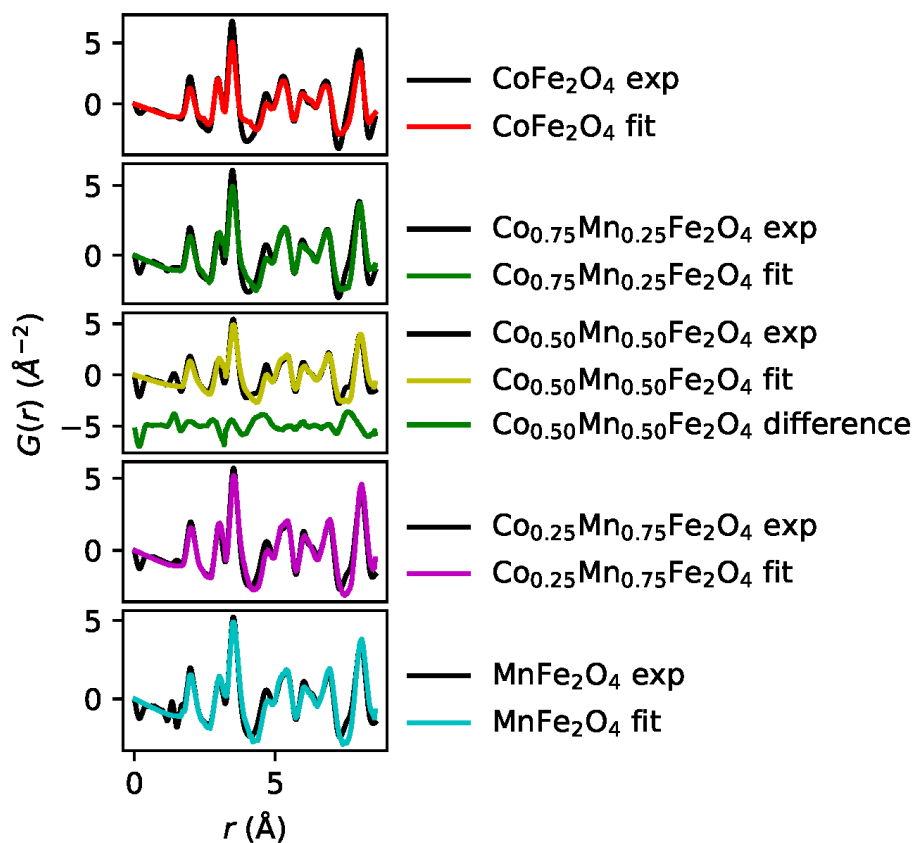


Figure 3. Comparison of the experimental and calculated $G(r)$.

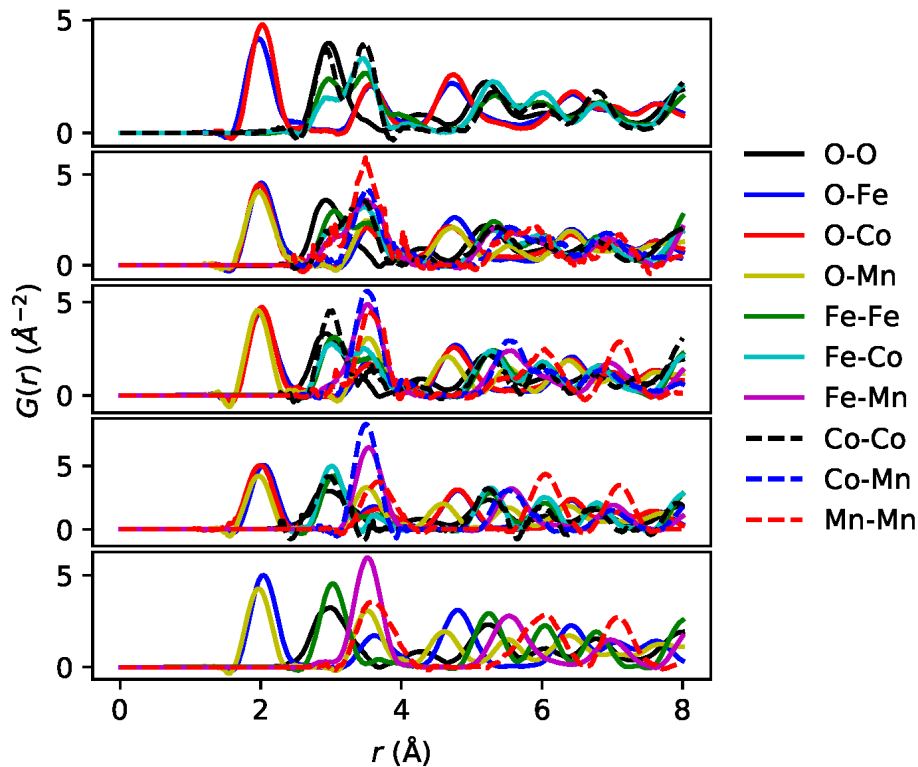


Figure 4. Partial PDFs corresponding to the fits in Figure 3.

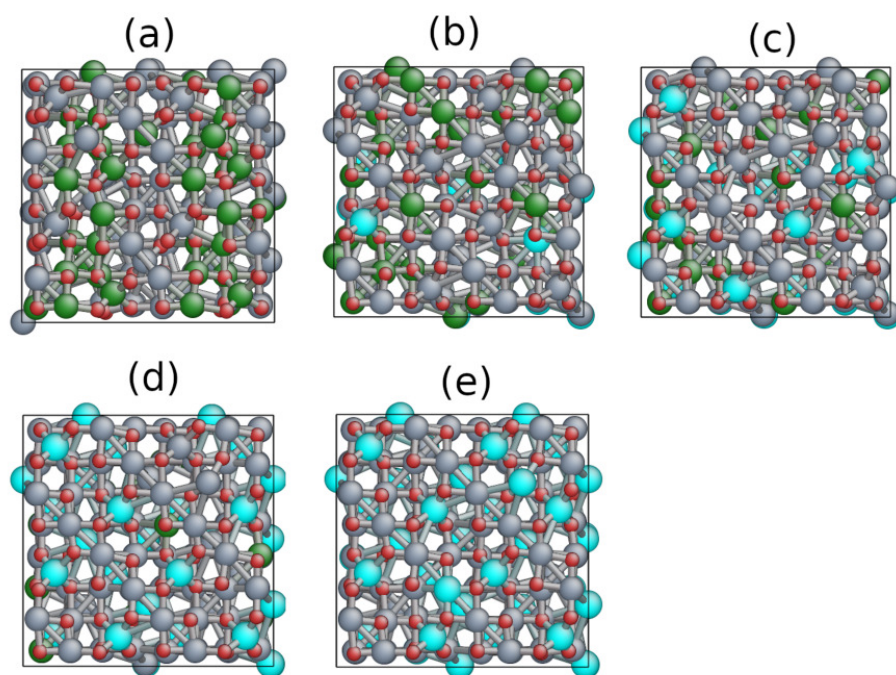


Figure 5. Optimized structures of all investigated samples. (a) CoFe_2O_4 , (b) $\text{Co}_{0.75}\text{Mn}_{0.25}\text{Fe}_2\text{O}_4$, (c) $\text{Co}_{0.50}\text{Mn}_{0.50}\text{Fe}_2\text{O}_4$, (d) $\text{Co}_{0.25}\text{Mn}_{0.75}\text{Fe}_2\text{O}_4$, (e) MnFe_2O_4 . O is red; Fe is gray; Co is green; Mn is cyan.

The peak around 1.20 \AA is the largest for $x = 0.5$ (red line). Clearly this feature is not captured by our RMC model, which does not include O_2 diatomic molecules; see the difference curve (green line) between theory and experiment shown in the third panel from the bottom in Figure 3. The O_2 sticking to the cobalt ferrite surface can be intuitively rationalized by the paramagnetic behavior of O_2 [23,45]. Notably, Barbiellini and Platzman [46] have suggested how ionized, activated, or excited molecules on semiconducting or metallic surfaces can quickly dissipate their excitations by coupling to the electron-hole spectrum of the material. This relaxation involves Auger-like processes and provides a “healing mechanism” to stabilize the sticking of molecules to the surface. In any event, our experiments suggest that Mn doping of $x = 0.5$ provides favorable conditions for O_2 diatomic molecules to stick to the surfaces of cobalt ferrite nanoparticles. The observed area of the peak related to the oxygen molecule can be explained in terms of the high surface-to-volume ratio [44], which results in many exposed octahedrally coordinated metal ions that can bind to oxygen molecules. We have verified that the oxygen molecule signal is a real feature and not an artifact of data processing by modifying the upper limit of the Fourier transform used in obtaining PDFs from the XRDs. Note that surface-molecule interactions contribute to the huge peak at around 2 \AA , which is associated with octahedral coordination. This large peak is not fitted perfectly by our model—a discrepancy that we attribute to the surface effects that are not included in our modeling.

4. Conclusions

We have determined the atomic structure of spinel cobalt ferrite nanoparticles doped with Mn on the basis of our HE-XRD measurements. Our analysis involved RMC modeling to obtain pair-distribution functions to fit our XRD experimental data. Our structural (atomic) models were consistent with the atomic configuration used in DFT calculations [5] that predict improved electron conduction and hence better bifunctional ORR/OER electrode properties of Mn-doped cobalt ferrite. Notably, our study has provided evidence for insulator/metal transitions adduced from the structural information. The RMC modeling in Figure 3 confirms that the salient features of the PDFs mostly reflect the bulk spinel atomic structure, in good agreement with the findings of Tian et al. [35]. The partial PDFs

in Figure 4 demonstrate that Co and Mn ions behave very differently in that they occupy different atomic sites in the spinel structure, as illustrated by the atomic distribution in Figure 5. Our PDF results at small distances suggest that the sticking of oxygen molecules to the surface of the ferrite nanoparticles stabilizes around a Mn doping of around $x = 0.5$. By yielding structural information about the cobalt ferrites at the atomic scale, our study will help accelerate the rational design of novel materials for metal–air batteries.

Author Contributions: Individual contributions: Conceptualization, S.K., R.K.C., B.B. and A.B.; methodology, K.D., C.O., J.M., K.K., H.Y., and S.K.; software, K.P. and K.O.; validation, K.P., B.B., A.B., and S.K.; formal analysis, K.P., K.O.; investigation, S.K.; resources; data curation, K.O., H.Y., and K.P.; writing—original draft preparation, K.P., B.B., and S.K.; writing—review and editing, K.P., B.B., S.K., A.B.; visualization, B.B., K.P., A.B., and S.K.; supervision, S.K., B.B., and A.B.; funding acquisition, S.K., B.B., and A.B. All authors have read and agreed to the published version of the manuscript.

Funding: The work at LUT university was supported by the Academy of Finland, grant number 326325. The work at Northeastern University was supported by the U.S. Office of Naval Research, grant number N00014-23-1-2330, and it benefited from Northeastern University’s Advanced Scientific Computation Center and the Discovery Cluster.

Data Availability Statement: The data that support the findings of this study are available from the corresponding authors upon reasonable request.

Acknowledgments: The authors wish to acknowledge CSC IT Center for Science, Finland, for computational resources. S.K. thanks the associate executive director at the University of Tennessee Space Institute, James Simonton, for providing support through an internal fund. The authors would like to thank Leif Karlsson for fruitful discussions regarding electronic structures and the proofreading of the manuscript. The HE-XRD experiments were performed with the approval of the Japan Synchrotron Radiation Research Institute (Proposal No.: 2011A1311).

Conflicts of Interest: The authors declare no conflict of interest.

References

1. Yin, J.; Shen, L.; Li, Y.; Lu, M.; Sun, K.; Xi, P. CoFe₂O₄ nanoparticles as efficient bifunctional catalysts applied in Zn–air battery. *J. Mater. Res.* **2018**, *33*, 590–600. [CrossRef]
2. Park, J.W.; Ju, Y.W. Evaluation of Bi-Functional Electrochemical Catalytic Activity of Co₃O₄-CoFe₂O₄ Composite Spinel Oxide. *Energies* **2023**, *16*, 173. [CrossRef]
3. Jia, Q.; Ramaswamy, N.; Hafiz, H.; Tylus, U.; Strickland, K.; Wu, G.; Barbiellini, B.; Bansil, A.; Holby, E.F.; Zelenay, P.; et al. Experimental observation of redox-induced Fe–N switching behavior as a determinant role for oxygen reduction activity. *ACS Nano* **2015**, *9*, 12496–12505. [CrossRef]
4. Nematollahi, P.; Barbiellini, B.; Bansil, A.; Lamoen, D.; Qingying, J.; Mukerjee, S.; Neyts, E.C. Identification of a Robust and Durable FeN₄C_x Catalyst for ORR in PEM Fuel Cells and the Role of the Fifth Ligand. *ACS Catal.* **2022**, *12*, 7541–7549. [CrossRef]
5. Hou, Y.; Yan, X.; Huang, Y.; Zheng, S.; Hou, S.; Ouyang, Y. Structural, electronic and magnetic properties of manganese substituted CoFe₂O₄: A first-principles study. *J. Magn. Magn. Mater.* **2020**, *495*, 165862. [CrossRef]
6. Sharma, K.; Calmels, L.; Li, D.; Barbier, A.; Arras, R. Influence of the cation distribution, atomic substitution, and atomic vacancies on the physical properties of CoFe₂O₄ and NiFe₂O₄ spinel ferrites. *Phys. Rev. Mater.* **2022**, *6*, 124402. [CrossRef]
7. Dileep, K.; Loukya, B.; Pachauri, N.; Gupta, A.; Datta, R. Probing optical band gaps at the nanoscale in NiFe₂O₄ and CoFe₂O₄ epitaxial films by high resolution electron energy loss spectroscopy. *J. Appl. Phys.* **2014**, *116*, 103505. [CrossRef]
8. Kohara, S.; Itou, M.; Suzuya, K.; Inamura, Y.; Sakurai, Y.; Ohishi, Y.; Takata, M. Structural studies of disordered materials using high-energy x-ray diffraction from ambient to extreme conditions. *J. Phys. Condens. Matter* **2007**, *19*, 506101. [CrossRef]
9. Ohara, K.; Onodera, Y.; Murakami, M.; Kohara, S. *J. Phys. Condens. Matter* **2021**, *33*, 383001. [CrossRef]
10. FIJI. Available online: <https://imagej.net/software/fiji/> (accessed on 2010).
11. Billinge, S.J. The rise of the X-ray atomic pair distribution function method: A series of fortunate events. *Philos. Trans. R. Soc. A* **2019**, *377*, 20180413. [CrossRef]
12. Faber, T.E.; Ziman, J.M. A theory of the electrical properties of liquid metals. *Philos. Mag. A J. Theor. Exp. Appl. Phys.* **1965**, *11*, 153–173. [CrossRef]
13. Harada, M.; Ikegami, R.; Kumara, L.S.R.; Kohara, S.; Sakata, O. Reverse Monte Carlo modeling for local structures of noble metal nanoparticles using high-energy XRD and EXAFS. *RSC Adv.* **2019**, *9*, 29511–29521. [CrossRef]
14. Warren, B. *X-ray Diffraction*; Dover Publications, Inc.: New York, NY, USA, 1969.
15. Egami, T.; Billinge, S. *Underneath the Bragg Peaks: Structural Analysis of Complex Materials*; Pergamon Press: Oxford, UK, 2003.
16. Billinge, S.J.L.; Levin, I. The problem with determining atomic structure at the nanoscale. *Science* **2007**, *316*, 561. [CrossRef]

17. Pradhan, S.K.; Deng, Z.T.; Tang, F.; Wang, C.; Ren, Y.; Moeck, P.; Petkov, V. Three-dimensional structure of Cd X (X = Se, Te) nanocrystals by total x-ray diffraction. *J. Appl. Phys.* **2007**, *102*, 044304. [[CrossRef](#)]
18. Fernández-García, M.; Belver, C.; Hanson, J.C.; Wang, X.; Rodriguez, J.A. Anatase-TiO₂ nanomaterials: Analysis of Key Parameters Controlling Crystallization. *J. Am. Chem. Soc.* **2007**, *129*, 13604–13612. [[CrossRef](#)]
19. Petkov, V. Nanostructure by high-energy X-ray diffraction. *Mater. Today* **2008**, *11*, 28. [[CrossRef](#)]
20. Bözin, E.S.; Malliakas, C.D.; Souvatzis, P.; Profferi, T.; Spaldin, N.A.; Kanatzidis, M.G.; Billinge, S.L. Entropically Stabilized Local Dipole Formation in Lead Chalcogenides. *Science* **2010**, *330*, 1660–1663. [[CrossRef](#)]
21. Jensen, K.M.Ø.; Bözin, E.S.; Malliakas, C.D.; Stone, M.B.; Lumsden, M.D.; Kanatzidis, M.G.; Shapiro, S.M.; Billinge, S.J.L. Lattice Dynamics Reveals a Local Symmetry Breaking in the Emergent Dipole Phase of PbTe. *Physical Rev.* **2012**, *B86*, 085313. [[CrossRef](#)]
22. Keen, D.A.; Goodwin, A.L. The crystallography of correlated disorder. *Nature* **2015**, *521*, 303. [[CrossRef](#)]
23. Deepak, F.L.; Bañobre-López, M.; Carbó-Argibay, E.; Cerqueira, M.F.; Piñeiro-Redondo, Y.; Rivas, J.; Thompson, C.M.; Kamali, S.; Rodríguez-Abreu, C.; Kovnir, K.; et al. A systematic study of the structural and magnetic properties of Mn-, Co-, and Ni-doped colloidal magnetite nanoparticles. *J. Phys. Chem. C* **2015**, *119*, 11947–11957. [[CrossRef](#)]
24. Mancini, A.; Malvasi, L. Recent advances in the application of total scattering methods to functional materials. *Chem. Commun.* **2015**, *51*, 16592. [[CrossRef](#)] [[PubMed](#)]
25. Jensen, K.M.Ø.; Blichfeld, A.B.; Bauers, S.R.; Wood, S.R.; Dooryhee, E.; Johnson, D.C.; Iversen, B.B.; Billinge, S.J.L. Demonstration of thin film pair distribution function analysis (tfPDF) for the study of local structure in amorphous and crystalline thin films. *IUCr* **2015**, *2*, 481–489. [[CrossRef](#)] [[PubMed](#)]
26. Jensen, K.M.; Juhas, P.; Tofanelli, M.A.; Heinecke, C.L.; Vaughan, G.; Ackerson, C.J.; Billinge, S.J. Polymorphism in magic-sized Au₁₄₄ (SR) 60 clusters. *Nat. Commun.* **2016**, *7*, 11859. [[CrossRef](#)] [[PubMed](#)]
27. Dippel, A.C.; Jensen, K.M.Ø.; Tyrsted, C.; Bremholm, M.; Bøjesen, E.D.; Saha, D.; Birgisson, S.; Christensen, M.; Billinge, S.J.L.; Iversen, B.B. Towards atomistic understanding of polymorphism in the solvothermal synthesis of ZrO₂ nanoparticles. *Acta Cryst.* **2016**, *A72*, 645–650.
28. Dippel, A.C.; Roelsgaard, M.; Boettger, U.; Schneller, T.; Gutowski, O.; Ruett, U. Local atomic structure of thin and ultrathin films via rapid high-energy X-ray total scattering at grazing incidence. *IUCr* **2019**, *6*, 290–298. [[CrossRef](#)]
29. Mathiesen, M.K.; Väli, R.; Härmäs, M.; Lust, E.; Bulow, J.F.; Jensen, K.M.Ø.; Norby, P. Following the in-plane disorder of sodiated hard carbon through operando total scattering. *J. Mater. Chem. A* **2019**, *7*, 11709. [[CrossRef](#)]
30. Christiansen, T.L.; Bøjesen, E.D.; Juulsholt, M.; Etheridge, J.; Jensen, K.M.Ø. Size induced structural changes in molybdenum oxide nanoparticles. *ACS Nano* **2019**, *13*, 8725–8735. [[CrossRef](#)]
31. Banerjee, S.; Liu, C.H.; Jensen, K.M.Ø.; Juhas, P.; D.Lee, J.; Tofanelli, M.; Ackerson, C.J.; Murray, C.B.; Billinge, S.J.L. Cluster-mining: an approach for determining core structures of metallic nanoparticles from atomic pair distribution function data. *Acta Cryst.* **2020**, *A76*, 24–31. [[CrossRef](#)]
32. Christiansen, T.L.; Cooper, S.R.; Jensen, K.M.Ø. There's no place like real-space: Elucidating size-dependent atomic structure of nanomaterials using pair distribution function analysis. *Nanoscale Adv.* **2020**, *2*, 2234–2254. [[CrossRef](#)]
33. Pussi, K.; Gallo, J.; Ohara, K.; Carb-Argibay, E.; Koleňko, Y.V.; Barbiellini, B.; Bansil, A.; Kamali, S. *Condens. Matter* **2020**, *5*, 19. [[CrossRef](#)]
34. Pussi, K.; Barbiellini, B.; Ohara, K.; Carbo-Argibay, E.; Kolen'ko, Y.V.; Bansil, A.; Kamali, S. Structural properties of PbTe quantum dots revealed by high-energy x-ray diffraction. *J. Phys. Condens. Matter* **2020**, *32*, 485401. [[CrossRef](#)] [[PubMed](#)]
35. Tiano, A.L.; Papaefthymiou, G.C.; Lewis, C.S.; Han, J.; Zhang, C.; Li, Q.; Shi, C.; Abeykoon, A.M.; Billinge, S.J.; Stach, E.; et al. Correlating size and composition-dependent effects with magnetic, mossbauer, and pair distribution function measurements in a family of catalytically active ferrite nanoparticles. *Chem. Mater.* **2015**, *27*, 3572. [[CrossRef](#)]
36. Michel, F.; Ehm, L.; Liu, G.; Han, W.; Antao, S.; Chupas, P.; Lee, P.; Knorr, K.; Eulert, H.; Kim, J.; et al. Similarities in 2- and 6-line ferrihydrite based on pair distribution function analysis of X-ray total scattering. *Chem. Mater.* **2007**, *19*, 1489–1496. [[CrossRef](#)]
37. McGreevy, R. Reverse Monte Carlo modelling. *J. Phys. Condens. Matter* **2001**, *13*, R877. [[CrossRef](#)]
38. Pussi, K.; Barbiellini, B.; Ohara, K.; Yamada, H.; Dwivedi, J.; Bansil, A.; Gupta, A.; Kamali, S. Atomic arrangements in an amorphous CoFeB ribbon extracted via an analysis of radial distribution functions. *J. Phys. Condens. Matter* **2021**, *33*, 395801. [[CrossRef](#)] [[PubMed](#)]
39. Pussi, K.; Louzguine-Luzgin, D.; Nokelainen, J.; Barbiellini, B.; Kothalawala, V.; Ohara, K.; Yamada, H.; Bansil, A.; Kamali, S. Atomic structure of an FeCrMoCBy metallic glass revealed by high energy x-ray diffraction. *J. Phys. Condens. Matter* **2022**, *34*, 285301. [[CrossRef](#)]
40. Erba, A.; Baima, J.; Bush, I.; Orlando, R.; Dovesi, R. Large-Scale Condensed Matter DFT Simulations: Performance and Capabilities of the CRYSTAL Code. *J. Chem. Theory Comput.* **2017**, *13*, 5019–5027. [[CrossRef](#)]
41. Tucker, M.G.; Keen, D.A.; Dove, M.T.; Goodwin, A.L.; Hui, Q. RMCProfile: Reverse Monte Carlo for polycrystalline materials. *J. Phys. Condens. Matter* **2007**, *19*, 335218. [[CrossRef](#)]
42. Sanna Angotzi, M.; Mameli, V.; Zakutna, D.; Kubaniova, D.; Cara, C.; Cannas, C. Evolution of the Magnetic and Structural Properties with the Chemical Composition in Oleate-Capped Mn_xCo_{1-x}Fe₂O₄ Nanoparticles. *J. Phys. Chem. C* **2021**, *125*, 20626–20638. [[CrossRef](#)]
43. Rushiti, A.; Hättig, C. Activation of Molecular O₂ on CoFe₂O₄ (001) Surfaces: An Embedded Cluster Study. *Chem.-Eur. J.* **2021**, *27*, 17115–17126. [[CrossRef](#)]

44. Pussi, K.; Barbiellini, B.; Ohara, K.; Yamada, H.; Carbo-Argibay, E.; Sousa, V.; Kolen'ko, Y.V.; Bansil, A.; Kamali, S. Structural Properties of Nanometer-Sized Gold Nanoparticles on a Silicon Substrate. *Phys. Status Solidi (B)* **2022**, *259*, 2100572. [[CrossRef](#)]
45. Dima, D.; Andrei, G. Interaction between ferrite particles and oxygen molecules within the polyester matrix of lightweight magnetic composites. *Rom. J. Phys.* **2004**, *49*, 795–806
46. Barbiellini, B.; Platzman, P. The healing mechanism for excited molecules near metallic surfaces. *New J. Phys.* **2006**, *8*, 20. [[CrossRef](#)]

Disclaimer/Publisher's Note: The statements, opinions and data contained in all publications are solely those of the individual author(s) and contributor(s) and not of MDPI and/or the editor(s). MDPI and/or the editor(s) disclaim responsibility for any injury to people or property resulting from any ideas, methods, instructions or products referred to in the content.